

Far infrared mapping of the gas cooling along the L1448 outflow^{*}

B. Nisini¹, M. Benedettini², T. Giannini^{1,2,3}, C. Codella², D. Lorenzetti¹, A.M. Di Giorgio², and J.S. Richer⁴

¹ Osservatorio Astronomico di Roma, 00040 Monteporzio Catone, Italy

² CNR-Istituto di Fisica dello Spazio Interplanetario, Area di Ricerca Tor Vergata, Via Fosso del Cavaliere, 00133 Roma, Italy

³ Istituto Astronomico, Università La Sapienza, Via Lancisi 29, 00161 Roma, Italy

⁴ Department of Physics, University of Cambridge, Cavendish Laboratory, Madingley Road, Cambridge CB3 0HE, UK

Received 6 April 2000 / Accepted 6 June 2000

Abstract. The molecular outflows associated with the two Class 0 sources L1448-mm and L1448-IRS3 have been mapped with the spectrometers on board the ISO satellite allowing to study in detail the physical and chemical structure of the shocked gas. The far infrared cooling is mainly due to the emission from pure rotational lines of CO, H₂O and H₂ excited at temperatures between 500 and 1200 K. [O I]63 μ m emission is also widely observed along the flows. Additional ground based observations of the ¹²CO 4-3 and 3-2 transitions in the surroundings of the L1448-mm source allow us to localize this warm emission in the extreme high velocity clumps forming the collimated molecular jet responsible for the entrainment of the outflow. Our analysis shows therefore that this jet is hotter than previously thought on the basis of millimeter observations alone.

A comparison with existing models suggests that the excitation along the outflow from L1448-mm is mainly due to low velocity ($V_s \leq 20 \text{ km s}^{-1}$) non-dissociative shocks (C-shocks) probably developed as the jet proceeds through a medium already put into motion by previous episodes of mass loss. Excitation from turbulent mixing layers along the molecular jet axis seems not able to explain the observed cooling ratios among the different molecular components.

An higher excitation shock component is likely present in the direction of the source L1448-IRS3, as testified by the detection of the [Si II] 35 μ m line and by a larger contribution of the [O I] emission.

Finally the abundance of gas-phase H₂O is largely enhanced with respect to its interstellar value all along the flow. Both the total luminosity of water and its abundance correlate with SiO at high excitation, implying that both H₂O and SiO are released in the low-velocity shocks developed along the outflow.

Key words: stars: formation – ISM: jets and outflows – ISM: individual objects: L1448-mm – ISM: individual objects: L1448N – infrared: ISM: lines and bands

Send offprint requests to: B. Nisini (bruni@coma.mporzio.astro.it)

^{*} Based on observations with ISO, an ESA project with instruments funded by ESA Member States (especially the PI countries: France, Germany, the Netherlands and the United Kingdom) with the participation of ISAS and NASA

1. Introduction

The flows from protostars proceed at high supersonic velocities producing strong shocks which compress, heat and put into motion the ambient medium. This, in turn, cools mainly radiatively through the emission from gas excited at different temperatures. The exact way in which this cooling is achieved strongly depends on the amount of protostellar energy transferred to the flow, on its acceleration mechanism and on the properties of the surrounding cloud. Therefore the observation of the radiation emitted by shock excited material along protostellar flows can be a powerful way to retrieve information about the mechanism at the origin of the outflows and indirectly also about the nature of their exciting source.

Shocks in protostellar outflows can be formed in a variety of different ways. In jet-driven outflow models, shocks can develop along the length of the jet in turbulent mixing layers (Cantó & Raga 1991) or at the head of the jet in the form of bow shocks able to sweep out the ambient material at large distances from the jet axis (Raga & Cabrit 1993; Chernin & Masson 1995). In models for outflows driven by collimated winds, shocks of different strengths can be formed as the whole wide angle shell directly impacts against the ambient medium (Hollenbach 1997).

All these mechanisms produce temperature gradients and different chemical structures along the flows. Therefore, a comprehensive view of the outflow process needs a sampling of the all components contributing to the cooling along with the definition of their physical properties. To achieve this goal it is essential a multiwavelength analysis ensuring a complete census of the different excitation components.

Emission of millimeter molecular lines (usually CO) at excitation temperatures of about 10-20 K is commonly used to probe the outflow large scale morphology and dynamics. This cold emission component is however commonly associated with much higher excitation conditions, usually localized along the outflow axis, and traced by molecular hydrogen vibrational lines (at $T_{\text{ex}} \sim 2000 \text{ K}$) or by optical and UV lines in Herbig-Haro objects (at $T_{\text{ex}} \sim 10^4 \text{ K}$). This hot gas is directly probing the shock interactions taking place along the flows (e.g. Reipurth & Raga 1999).

Observations performed with the Infrared Space Observatory (ISO, Kessler et al. 1996) have allowed to identify the pres-

ence of gas excited at temperatures intermediate between those sampled by ground based observations, i.e. 100–2000 K (Liseau et al. 1996; Nisini et al. 1998). The contribution to the gas cooling due to this “warm” gas is not at all negligible and often represents a significant fraction of the total shock luminosity emitted along the flow (Nisini et al. 1999a; Benedettini et al. 2000). The presence of warm gas has been identified also by means of ground-based observations of CO lines at higher excitation (Hatchell et al. 1999). However, as also pointed out in those works, it is difficult to constrain the warm gas conditions by means of ratios between lines having excitation temperatures much lower than the traced kinetic temperature.

We report here a detailed study conducted with the ISO spectrometers towards the L1448 outflow. This outflow is one of the first well studied examples of strong and well collimated flows emitted from a so called Class 0 protostar (André et al. 2000). This exciting source (called L1448-mm or L1448-C) is an isolated millimeter source strongly emitting also at radio wavelength and in water masers (Curiel et al. 1990; Chernin 1995). North of this main outflow is located an IRAS source, originally named IRS3, which has been separated in two distinct peaks (Barsony et al. 1999; Chandler & Richer 2000) i.e. L1448-N and NW, the first of which dominates over all the millimeter emission of the cluster. A second outflow originates from this cluster, which overlaps and interacts with the main outflow from L1448-mm. A recent, large field H₂ map of the L1448 region, shows that this second outflow may actually be more extended than previously recognized (Eisloffel 2000). The L1448-mm outflow is characterized by the presence of a very collimated jet consisting of well separated extreme high-velocity (EHV, i.e. more than 50 km s⁻¹) molecular clumps (“bullets” following Bachiller et al. 1990, hereafter B90). CO at lower velocity delineates a biconical cavity which has been probably created by the material swept out from the molecular jet (Bachiller et al. 1995); the H₂ emission morphology as well suggests that the collimated jet is entraining the ambient material through successive bow shocks developed at its head (Bally et al. 1993; Davis et al. 1994).

In a previous paper (Nisini et al. 1999b, hereafter Paper I), we have shown that a strong contribution to the gas cooling in the surroundings of the mm source is accomplished through emission of H₂O and high-J CO lines at a temperature in excess of 700 K. It has also been suggested that such a warm gas is originated in shocks developed along the molecular bullets close to the mm source, indicating that the temperature of the EHV jet can in fact reach values much larger than previously thought.

In this paper we complement the ISO observations presented in Paper I with ground based measurements of high-J (4-3, 3-2) CO transitions in order to better constrain the physical conditions in the innermost parts of the molecular jet. In addition, we present several ISO spectra from mid- to far-infrared taken in different positions of the outflow, including a position centered on IRS3, which will be used to characterize the physical and chemical structure of the flow and to define its main cooling channels.

2. Observations and results

2.1. ISO

The two ISO spectrometers (Short Wavelength Spectrometer, SWS, de Graauw et al. 1996, and Long Wavelength Spectrometer, LWS, Clegg et al. 1996) have been used to observe different positions along the L1448 outflow. In Fig. 1 we show the pointings of the two instruments, together with their focal plane apertures, superimposed on a H₂ 2.12 μm image of the region taken from Davis & Smith (1995). We have targetted six different positions; two of them are centered on the two Class 0 sources L1448-mm and IRS3. This latter, which corresponds to the IRAS source 03225+3034, is actually separated into three different objects associated with peaks of millimeter continuum emission (Terebey & Padgett 1997; Barsony et al. 1999). The IRS3 position is close to the strongest of these peaks, corresponding to the binary L1448-N(A) and N(B). The LWS field of view (~ 80'' in diameter) includes also the northeast source L1448-NW which is, on the contrary, missed by the smaller SWS beam (which has values of 14'' × 20'', 14'' × 27'' or 20'' × 33'', depending on the wavelength). The other pointings are located both in the blue (referred as BI) and in the red (referred as RED, RI and RII) lobes of the outflow.

We clearly see from the figure that, due to the different beam-size, the two instruments sample different regions along the flow. In particular, the six LWS measurements overlap each other by about half of the beam, while the SWS observations heavily undersample the region. This fact needs to be taken in mind when comparing the results from the two instruments.

The observational procedure and the results obtained for the L1448-mm spectrum are fully described in Paper I. In Table 1 we report the journal of the observations for all the other measurements including coordinates of the pointed positions (Columns 2 and 3), observing mode, orbit and date of each measurement (Columns 4,5 and 6) and the total integration time of the observations (Column 7).

With LWS we obtained full scans (43–197 μm) at low resolution (R~200), oversampling by a factor of four the resolution element (which is 0.29 μm for λ < 90 μm and 0.6 μm for λ ≥ 90 μm). Each spectral sample was integrated for 4.8 s; this integration time was obtained by performing 12 different full scans with 0.4 s integration each. SWS in its grating mode SWS02 has been used to scan the (0-0) H₂ lines from S(1) to S(7) (with a beamsize of 14'' × 20'' for the lines from S(2) to S(7) and 14'' × 27'' for the S(1) line) and the [Si II] 35 μm (with a beamsize of 20'' × 33'') with a resolution ranging from 1000 to 2000. Each line was integrated for 200 s. The LWS spectra were reduced using the standard pipeline version 7, while the SWS data were reduced with the interactive analysis software OSIA¹. The final average of the various spectra and cleaning for spurious signals have been performed with the ISO analysis software ISAP

¹ OSIA is a joint development of the SWS consortium. Contributing institutes are SRON, MPE, KUL and the ESA Astrophysics Division.

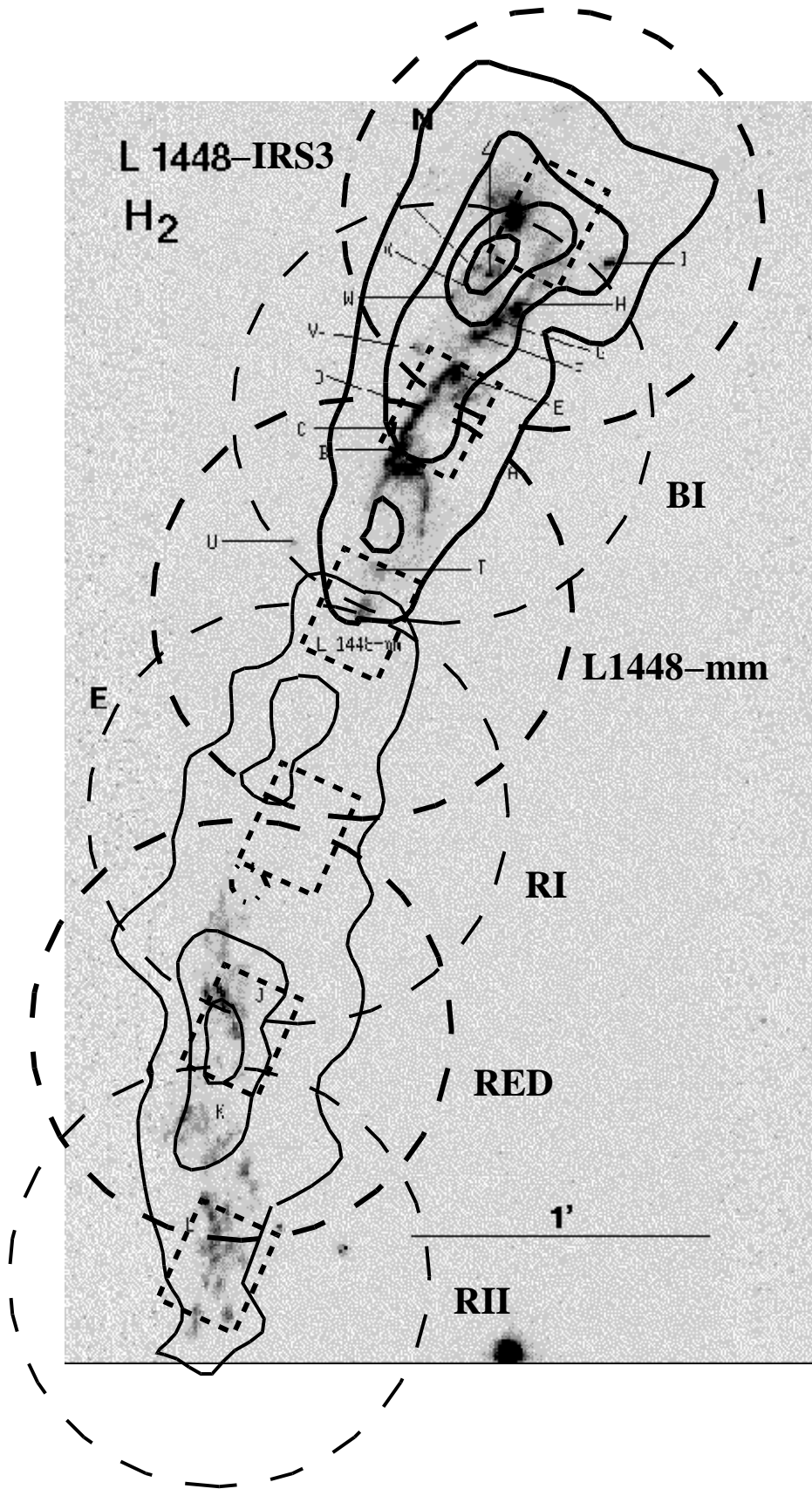


Fig. 1. Narrow-band image of the L1448 outflow at $2.12\mu\text{m}$ (H_2 +continuum) from Davis & Smith (1995) with superimposed the LWS (long-dashed circles) and SWS (short-dashed rectangles) beams on the targetted positions. For SWS only the smallest field of view of $14'' \times 20''$ is shown. The various observed positions are labelled as defined in the text. The thick and thin solid lines delineate respectively the contours of the blue- and red-shifted CO outflow from the L1448-mm source (adapted from Bachiller et al. 1990).

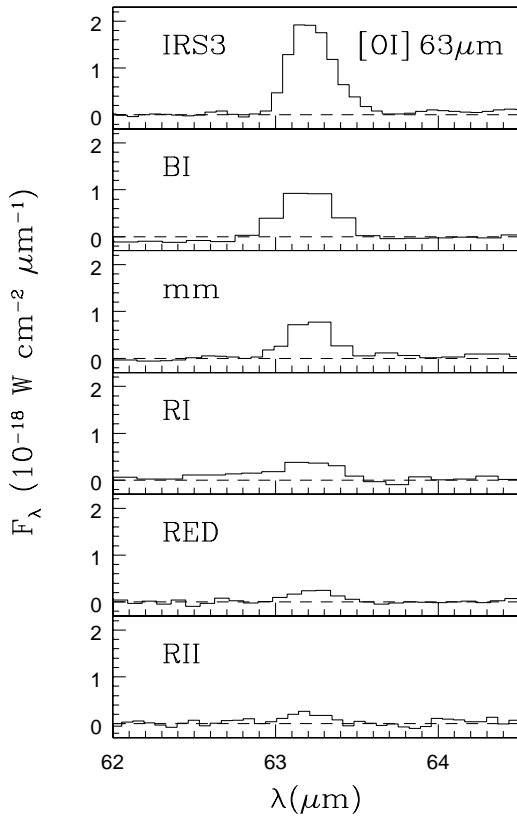


Fig. 2. Observed [O I] 63 μm line in all the positions pointed by LWS. The different positions are named as in Fig. 1.

v.1.6a². The final absolute flux calibration error due to this process results to be better than 30%. LWS spectra on the positions BI and RI, having strong off-axis emission due to the presence of the two Class 0 sources at the edge of the beam, are affected by the presence of interference fringes (Swinyard et al. 1996), thus routines available inside ISAP have been used to correct for this effect. Finally, line fluxes have been calculated by single or double (in presence of blendings) gaussian fitting. The statistical errors on the line intensity correspond to 1σ uncertainty derived from the rms fluctuations of the local baseline. In Tables 2 and 3 we report the parameters of the lines detected with LWS and SWS respectively, together with their identified transitions. For the LWS data, the difference between the observed and rest wavelength is always less than half the resolution element, with few exceptions which are marked on Table 2. In the same table are reported also some upper limits used during the analysis.

A view on how the different line emission varies along the flow is given in Figs. 2 and 3 where we show the continuum subtracted spectra of [O I] 63 μm and H₂ rotational lines in all the observed positions (including L1448-mm), while in Fig. 4 we have plotted the spectrum from 100 to 190 μm of IRS3, the mm source and the RED position, which are the three independent

² The ISO Spectral Analysis Package (ISAP) is a joint development by the LWS and SWS Instrument Teams and Data Centers. Contributing institutes are CESR, IAS, IPAC, MPE, RAL and SRON.

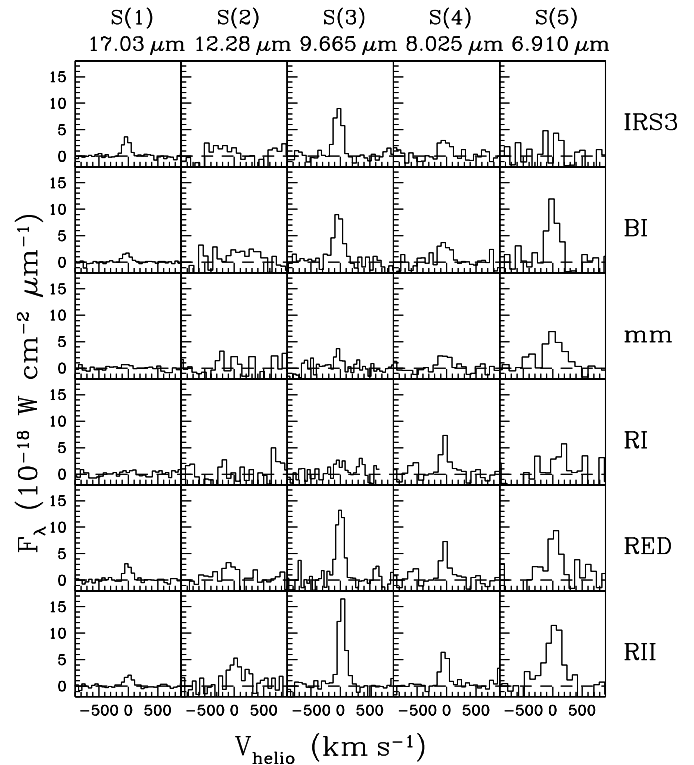


Fig. 3. Continuum subtracted SWS spectra of the (0-0) H₂ lines. We also plot the spectra in positions where no line emission has been detected to show the intensity gradients along the flow.

pointings performed with LWS. From the tables and figures, there are some features which can be noticed. First of all there is a clear decrease in the O I emission going from the IRS3 source to the red lobe which is not followed by the H₂ emission; the H₂ lines have a minimum of intensity south of the mm source (in the RI position) and increase again towards the peak of the red lobe. [Si II] 35 μm and [O I] 145 μm are detected only in the IRS3 position. Finally, Fig. 4 shows that the two Class 0 sources present slightly different spectra; although some H₂O lines are observed towards IRS3, the water spectrum is not so rich as in the mm source. Some fairly intense water lines are also observed in the red lobe of the outflow together with few CO lines (J_{up} 16, 17 and 18).

2.2. JCMT

Small maps in the ¹²CO 4-3 (461.041 GHz) and ¹²CO 3-2 (345.796 GHz) around L1448-mm have been obtained at the James Clerk Maxwell Telescope (JCMT) on July 24th, 1999; additional spectra were also acquired on August 12th, 1999 as part of the JCMT Service Observing Programme. The used instruments were the heterodyne receivers RxW in the C band (bandwidth = 12'') and RxB3 (bandwidth = 14'') for the 460 GHz and the 350 GHz respectively. The 4-3 observations were carried out with an atmospheric opacity at 225 GHz of the order of 0.1 or less. The measurements were performed making grid maps of 5 × 3 and 7 × 5 points for the CO 4-3 and 3-2 respectively, with

Table 1. Journal of observations.

| Source | $\alpha(2000)$ | | | $\delta(2000)$ | | | AOT | # orbit | Date | t_{obs} sec |
|------------|----------------|----------|----------|----------------|----------|-----------|-------|---------|-----------|------------------|
| | <i>h</i> | <i>m</i> | <i>s</i> | <i>°</i> | <i>'</i> | <i>''</i> | | | | |
| L1448-IRS3 | 3 | 25 | 36.0 | +30 | 45 | 19.5 | LWS01 | 653 | 30 Aug 97 | 2590 |
| | | | | | | | SWS02 | 814 | 06 Feb 98 | 1730 |
| L1448-BI | 3 | 25 | 37.4 | +30 | 44 | 42.5 | LWS01 | 653 | 29 Aug 97 | 2590 |
| | | | | | | | SWS02 | 816 | 08 Feb 98 | 1730 |
| L1448-RI | 3 | 25 | 40.1 | +30 | 43 | 24.3 | LWS01 | 653 | 29 Aug 97 | 2590 |
| | | | | | | | SWS02 | 847 | 11 Mar 98 | 1730 |
| L1448-RED | 3 | 25 | 41.4 | +30 | 42 | 44.0 | LWS01 | 653 | 30 Aug 97 | 2590 |
| | | | | | | | SWS02 | 847 | 11 Mar 98 | 1730 |
| L1448-RII | 3 | 25 | 41.4 | +30 | 41 | 59.2 | LWS01 | 653 | 30 Aug 97 | 2590 |
| | | | | | | | SWS02 | 816 | 08 Feb 98 | 1730 |

Table 2. Emission lines measured with LWS

| Line id. | λ_{vac} (μm) | L1448-IRS3 | BI | RI | RED | RII |
|---|--------------------------------------|--|-----------------|----------------|----------------|----------------|
| | | $F \pm \Delta F^a$ ($10^{-20} \text{ W cm}^{-2}$) | | | | |
| [O I] $^3P_1 \rightarrow ^3P_2$ | 63.18 | 66 \pm 1.5 | 39.7 \pm 2.4 | 14.6 \pm 2.3 | 9.0 \pm 2.2 | <9 |
| o-H ₂ O 5 ₀₅ -4 ₁₄ | 99.49 | | 8.3 \pm 2.5 | | | |
| CO 25-24 | 104.44 | 5.5 \pm 1.4 ^b | | | | |
| o-H ₂ O 2 ₂₁ -1 ₁₀ | 108.07 | {5.2 \pm 1.3 | {6.8 \pm 2.0 | {6.7 \pm 1.0 | {3.2 \pm 0.7 | {2.3 \pm 0.6 |
| CO 24-23 | 108.76 | | | | | |
| CO 23-22 | 113.46 | {5.2 \pm 1.3 | {12.0 \pm 3.2 | {5.7 \pm 1.0 | {3.3 \pm 0.6 | {2.5 \pm 0.6 |
| o-H ₂ O 4 ₁₄ -3 ₀₃ | 113.54 | | | | | |
| CO 21-20 | 124.19 | | 6.1 \pm 1.7 | | | |
| p-H ₂ O 4 ₀₄ -3 ₁₃ | 125.35 | | 2.8 \pm 0.8 | | | |
| o-H ₂ O 5 ₁₄ -5 ₀₅ | 134.93 | | 6.7 \pm 1.4 | | | |
| CO 19-18 | 137.20 | 3.1 \pm 0.5 | 5.6 \pm 1.6 | | | |
| p-H ₂ O 3 ₁₃ -2 ₀₂ | 138.53 | | 4.6 \pm 1.4 | | | |
| CO 18-17 | 144.78 | 4.2 \pm 0.9 | 4.8 \pm 1.4 | 3.3 \pm 1.1 | 1.5 \pm 0.4 | |
| [O I] $^2P_3 \rightarrow ^2P_2$ | 145.52 | 4.5 \pm 1.2 | | | | |
| CO 17-16 | 153.27 | 8.1 \pm 1.0 | 8.8 \pm 1.5 | 3.6 \pm 0.9 | 1.3 \pm 0.3 | <1.6 |
| [C II] $^2P_{3/2} \rightarrow ^2P_{1/2}$ | 157.74 | 7.4 \pm 1.0 | 9.5 \pm 0.9 | 5.1 \pm 0.9 | 5.5 \pm 0.4 | 8.5 \pm 0.7 |
| CO 16-15 | 162.81 | 8.0 \pm 1.2 | 6.6 \pm 1.1 | 3.4 \pm 0.8 | 1.4 \pm 0.5 | <2 |
| CO 15-14 | 173.63 | 10.2 \pm 2.0 | 9.6 \pm 1.9 | 4.6 \pm 1.4 | <2.9 | |
| o-H ₂ O 3 ₀₃ -2 ₁₂ | 174.63 | 4.6 \pm 1.0 | 9.6 \pm 1.9 | 7.9 \pm 1.4 | 4.17 \pm 1.0 | 3.0 \pm 0.7 |
| o-H ₂ O 2 ₁₂ -1 ₀₁ | 179.53 | 4.9 \pm 1.5 | 10.4 \pm 1.8 | 12.4 \pm 1.8 | 7.8 \pm 1.0 | 8.2 \pm 1.8 |
| CO 14-13 | 186.00 | 13.0 \pm 2.3 | 8.9 \pm 1.8 | <6.0 | <4.0 | |

^a Errors are statistical and upper limits are at the 3σ level.

^b Difference between the observed wavelength and λ_{vac} exceeding half the resolution element.

Table 3. Emission lines measured with SWS

| Line id. | λ_{vac} (μm) | L1448-IRS3 | BI | RI | RED | RII |
|-----------|--------------------------------------|--|---------------|---------------|----------------|----------------|
| | | $F \pm \Delta F^a$ ($10^{-20} \text{ W cm}^{-2}$) | | | | |
| (0-0)S(7) | 5.5112 | <3.3 | <3.9 | <2.3 | <4.0 | <2.2 |
| (0-0)S(6) | 6.1086 | <2.2 | <2.4 | <2.5 | <2.5 | <2.0 |
| (0-0)S(5) | 6.9095 | <4 | 6.2 \pm 1.0 | <2.8 | 4.1 \pm 0.95 | 8.8 \pm 0.2 |
| (0-0)S(4) | 8.0251 | 5.8 \pm 0.4 | 2.3 \pm 0.6 | 1.3 \pm 0.4 | 2.8 \pm 0.44 | 2.9 \pm 0.28 |
| (0-0)S(3) | 9.6649 | 5.4 \pm 0.4 | 6.2 \pm 0.7 | <1.8 | 7.1 \pm 0.5 | 8.2 \pm 0.4 |
| (0-0)S(2) | 12.279 | <7.8 | <2.4 | <5.5 | <5.6 | 4.5 \pm 1.5 |
| (0-0)S(1) | 17.035 | 3.1 \pm 0.26 | 1.7 \pm 0.2 | <1.4 | 2.6 \pm 0.3 | 2.0 \pm 0.27 |
| [Si II] | 34.814 | 5.8 \pm 1.3 | <2.4 | <2.9 | <2.6 | <2.0 |

^a Errors are statistical and upper limits are at the 3σ level

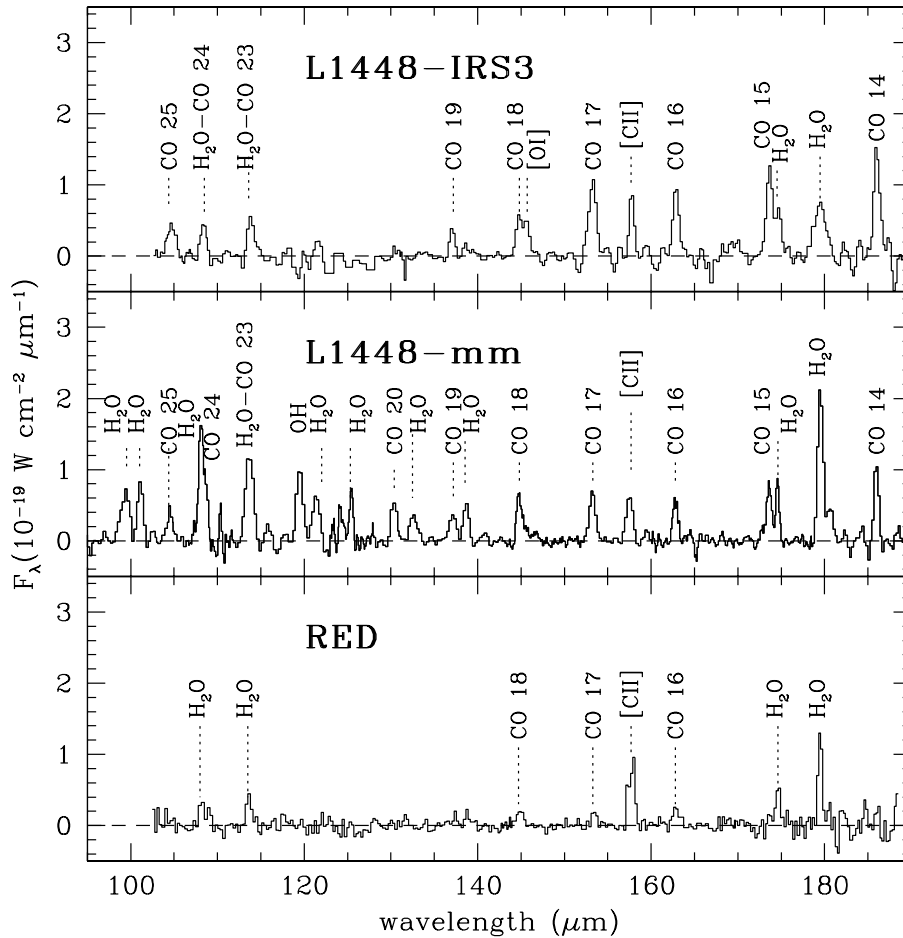


Fig. 4. Portions of the continuum subtracted LWS spectra of the two sources L1448-IRS3 and L1448-mm, and of the outflow red lobe (position RED).

a $10''$ spacing, oriented along the flow (P.A. = 157.4°). Such a grid comprises the extreme high velocity (EHV) bullets named R1 and B1 by B90, and it roughly covers the part of the flow observed with LWS towards the mm source pointing. Beam-switching was employed to cancel sky emission, using a throw of $180''$ oriented in a direction perpendicular to the L1448 outflow axis. The backend was the digital autocorrelation spectrometer (DAS) set up with a bandwidth of 500 MHz. The system temperature during the observations was about $T_{\text{sys}} = 800$ K for the B3 receiver and $T_{\text{sys}} = 2500$ K and 1600 K for the W receiver during the two nights in July and August respectively. To convert the antenna temperature (T_A) into brightness temperature, a main beam efficiency η_{MB} equal to 0.7 was adopted for receiver B3. Since the RxW efficiency was not well known at the time of the observations, spectra of Mars and Uranus were obtained during the different runs and the measured η_{MB} was 0.40 ± 0.05 . Pointing sources were W3(OH) and NGC7538 IRS1, which was also used as a secondary calibrator. Pointing accuracy was about $3''$.

In Fig. 5 we show the spectra obtained close to the mm source. From this figure we clearly see, in addition to the high velocity wings, the presence of the EHV gas bullets having a global velocity of about 60 km s^{-1} . Contour maps of the CO 3-2 and 4-3 line intensity integrated over the velocity intervals relative to these bullets are plotted in Fig. 6. These maps show that the bullets are partially resolved by the JCMT beam along

the flow axis direction with an elongation of about $20''$ while remain unresolved in the direction perpendicular to it. Since our primary aim is to compare the emission from such bullets with the ISO-LWS CO emission, we have computed their absolute intensity by fitting their profiles which result to be gaussian to a good approximation. The resulting values integrated in the bullets emission area are given in Table 4 for the red- and blue-shifted gas.

3. Properties of the warm gas

The H_2 (0-0) lines are very good thermometers of warm gas. Being originated from quadrupole transitions, they have low values of radiative coefficients implying that they are optically thin and thermalized as soon as the density exceeds values of $\sim 10^3 \text{ cm}^{-3}$. The gas temperature can be derived using an excitation diagram in which the natural logarithm of the column density of the upper level population, divided by its statistical weight, is plotted as a function of the energy of the level E_j . Under LTE, these two quantities are related by a linear relationship, in which the kinetic temperature is given by the reciprocal of the angular coefficient. To construct the excitation diagrams for each of the observed positions, we have taken the spontaneous radiative rates from Turner et al. (1977), while an ortho-to-para- H_2 equal to 3 was adopted. The validity of this lat-

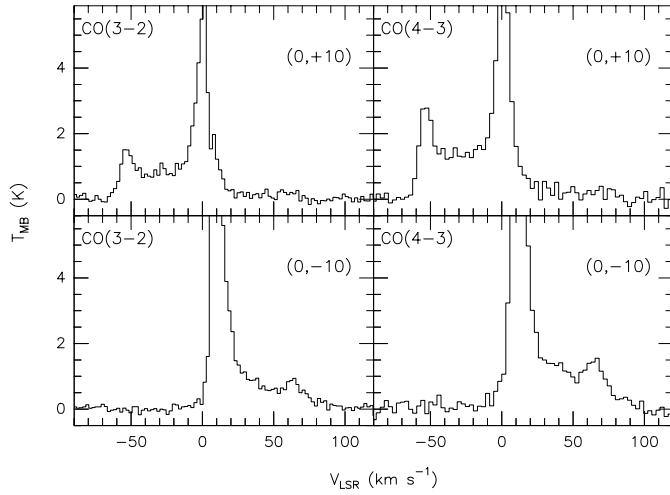


Fig. 5. ^{12}CO 3-2 and ^{12}CO 4-3 spectra of the blue- and red-shifted peaks of EHV gas in the surroundings of L1448-mm.

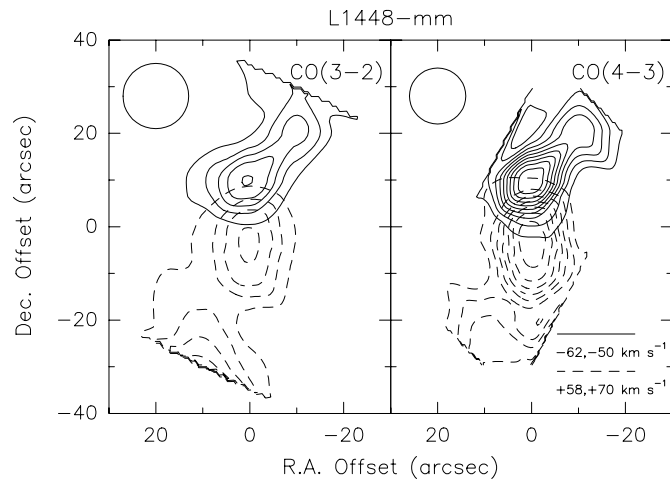


Fig. 6. Maps of the CO 3-2 and 4-3 line intensity integrated in the velocity intervals from -62 to -50 km s^{-1} and from 58 to 70 km s^{-1} for the blueshifted (solid contours) and redshifted (dashed contours) emission respectively. The instrumental beams are reported in the upper left corner of each diagram. For both maps, the first contour is at 2.5 K km s^{-1} (about 5σ from the rms noise) which is also the value of the contour intervals. Offsets are with respect to L1448-mm ($\alpha_{2000} = 3^{\text{h}} 25^{\text{m}} 38^{\text{s}}.8$, $\delta_{2000} = 30^{\circ} 44' 05''$).

ter assumption has been checked *a posteriori* by verifying that the observed (ortho and para) transitions do not appear shifted relative to each other once plotted in the excitation diagram. When calculating the column densities, no correction for the beam-filling has been applied since all the lines but the S(1) are observed with the same aperture and the beam size of the S(1) observation is only about 30% higher.

Given the particular sensitivity of the S(3) line at 9.7 μm to the extinction correction, due to its location inside the silicate band, we have not included this line in the construction of the excitation diagram. We have instead used it to give an estimate of the extinction by imposing that it should stay on the same straight line defined by the other transitions. For this purpose,

Table 4. Parameters of the gaussian fits to the CO 4-3 and CO 3-2 emission relative to the EHV components. The error is given by the residuals of the fit.

| | $\int T_{MB} dv$ K km s^{-1} | Error K km s^{-1} | v_{LSR} km s^{-1} | Δv km s^{-1} |
|----------------------|--|-------------------------------|---------------------------------|----------------------------------|
| ^{12}CO 4-3 | | | | |
| red lobe | 27.7 | 1.3 | 64.0 | 12.5 |
| blue lobe | 35.7 | 3.2 | -54.0 | 11.9 |
| ^{12}CO 3-2 | | | | |
| red lobe | 11.84 | 0.9 | 63.1 | 9.7 |
| blue lobe | 18.4 | 1.1 | -53.3 | 9.7 |

we have used the $A_{9.7\mu\text{m}}/A_V$ value given by Rieke & Lebofsky (1985). This A_V estimate is affected by a 50% of relative error due to the uncertainty on the extinction curve at this wavelength (see e.g. Draine 1989). Finally, a range of temperatures has been derived from each plot, considering the straight lines with the maximum and minimum slopes compatible with the statistical errors associated at each line flux.

In Fig. 7, these excitation diagrams are shown for all the observed positions but the RI pointing, where only one transition has been detected. An upper limit of 800 K in the position RI is obtained by comparing the detected S(4) line flux with the upper limits in the other transitions; consequently, a lower limit of 8.6 mag on the A_V is derived. In Fig. 7 we also report, for comparison, the diagram relative to the observations on L1448-mm taken from Paper I. Finally, the derived temperature and extinction values are listed in Table 5. We note that, with the exception of the mm source position where the temperature rises above 1000 K, there are no strong gradients along the flow and the temperature is maintained at values between 500 and 800 K. The extinction appears to be higher towards the mm source (11–16 mag) and in the RI position, while there is not a significant increase of extinction towards the position of IRS3 (6–9 mag), despite a mm map of the region shows that the IRS3 core has definitely an higher column density with respect to the mm source (Barsony et al. 1999). This may indicate that the H_2 lines do not originate from the innermost part of the core.

Beam-averaged column densities are listed in Table 5; these have to be considered as a lower limit on the true values since we do not know the real size of the emitting region.

CO and H_2O line emission has been analysed using a Large Velocity Gradient model in a plane-parallel geometry. The details of this model together with the procedure to derive the main physical parameters are fully described in Paper I. Very briefly, we take the temperature as derived from the H_2 lines analysis and use the CO line ratios to give an estimation of the volume density. We then apply these values of T and n_{H_2} to the water lines in order to derive, from their ratios and absolute intensities, both the column density and the size of the emitting region. Finally, if we assume that CO and water are emitted in a region of the same size, we can also derive a CO column density.

In Table 5 we list all the physical parameters derived from the procedure described above.

Table 5. Physical parameters

| | L1448-IRS3 | BI | mm | RI | RED | RII |
|------------------------|--------------|---------------|-------------|----------------|----------------|----------------|
| $T(K)$ | 500–600 | 700–750 | 1200 | 700–800 | 600–650 | 700–850 |
| $n_{H_2} (cm^{-3})$ | $(1-2) 10^5$ | $(1-2) 10^5$ | $6 10^4$ | $(0.6-1) 10^5$ | $(1-3) 10^4$ | $(0.8-3) 10^4$ |
| $A_V (mag)$ | 6–9 | 4–6 | 11–16.5 | >8.6 | 4.7–7 | 4–6 |
| $\Omega(sr)$ | $4 10^{-10}$ | $8 10^{-10}$ | $3 10^{-9}$ | $3 10^{-9}$ | $2 10^{-9}$ | $5 10^{-9}$ |
| $N_{CO} (cm^{-2})^a$ | $7 10^{17}$ | $1 10^{17}$ | $8 10^{16}$ | $7 10^{16}$ | $\sim 10^{17}$ | $< 10^{17}$ |
| $N_{H_2O} (cm^{-2})^a$ | $2 10^{17}$ | $1 10^{17}$ | $4 10^{17}$ | $7 10^{16}$ | $\sim 10^{17}$ | $\sim 10^{17}$ |
| $N_{H_2} (cm^{-2})^b$ | $4 10^{19}$ | $1.5 10^{19}$ | $3 10^{18}$ | $6 10^{18}$ | $5 10^{19}$ | $3 10^{19}$ |

^a Column densities computed assuming the emitting areas given in the table.

^b Column densities averaged in the SWS beam.

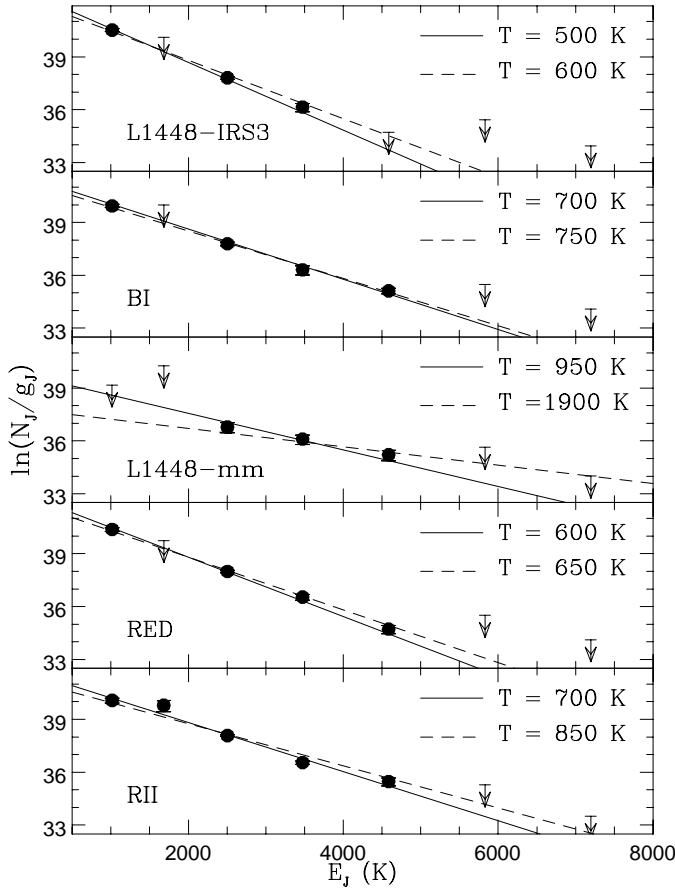


Fig. 7. H_2 excitation diagrams for the five pointed positions in which three or more lines have been detected. The statistical errors of the measurements are less or about the plot symbol. The full and dashed lines represent respectively the Boltzmann distributions at the minimum and maximum temperature compatible with the data.

For L1448-mm, the CO 4-3 and 3-2 data obtained at JCMT have been used to check the consistency of the hypothesis that the high- J CO emission observed by ISO comes mainly from the EHV bullets and, at the same time, to constrain the range of parameters derived in Paper I. Fig. 8 shows the result of the obtained fit: a temperature of 1200 K and a density of $6 10^4 cm^{-3}$ are derived, which are fully compatible with the range of parameters estimated from the LWS data alone, i.e. $T = 700-$

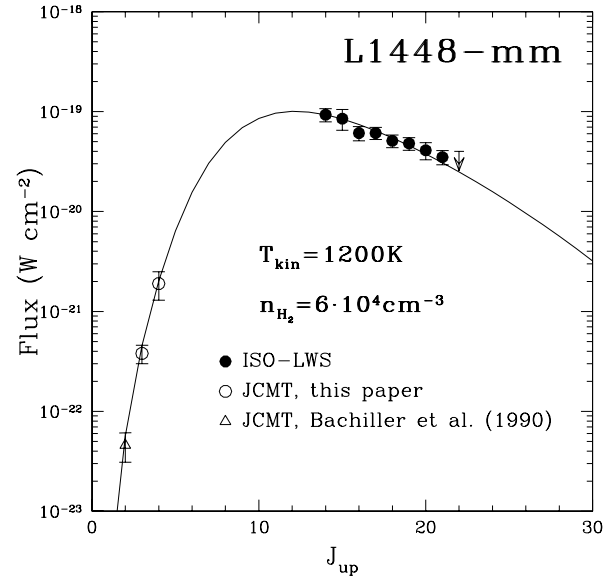


Fig. 8. Flux of the CO transitions observed towards L1448-mm by ISO ($J_{up} > 14$ filled circles) and by JCMT ($J_{up} = 2,3,4$ open circles) as a function of the rotational quantum number. The full line represents the best fit through the data obtained with the LVG model.

1400 K and $n_{H_2} = (0.3-5) 10^4 cm^{-3}$ (Paper I). Moreover, the obtained model fit gives optical depths always less than 0.01 for all the lines. Since with the JCMT beam we partially resolve the emitting area, we can effectively derive the CO column density from the 4-3 and the 3-2 line fluxes without the beam filling problems affecting the LWS data; the resulting value is $N_{CO} \sim 8 10^{16} cm^{-2}$. The corresponding mass for each of the red- and blue-shifted bullets is about $3 10^{-3} M_{\odot}$ (for a CO abundance of about 10^{-4}). This is more than a factor of ten higher than the mass estimated by B90 assuming a temperature of about 20 K.

Fig. 9 shows the fit to the CO data obtained for the IRS3 source. The density derived is $\sim 2 10^5 cm^{-3}$, assuming the temperature of ~ 550 K derived from H_2 .

As seen for the mm source in Paper I, also the IRS3 spectrum indicates the presence of two distinct components once we plot the CO line fluxes as a function of the upper level rotational quantum number, with the transitions with $J_{up} > 23$ lying above the fit obtained with the other lines. The situation is in

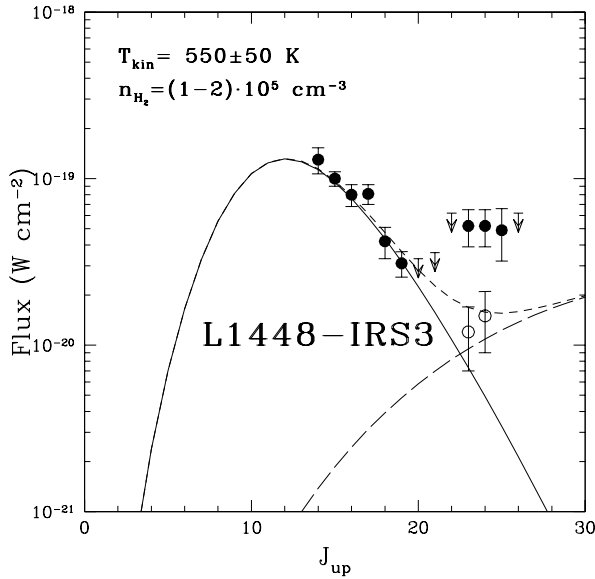


Fig. 9. Flux of the CO transitions observed towards L1448-IRS3 (filled circles) as a function of the rotational quantum number. The full line represents the best fit through the transitions with J_{up} from 14 to 19. The open circles are the CO fluxes of the $J_{\text{up}} = 23$ and 24 transitions after the subtraction of the expected contribution of the closely $4_{14}-3_{03}$ and $2_{21}-1_{10}$ H_2O lines. The long- and short-dashed lines represent an LTE gas at $T = 2000$ K and its convolution with the $T = 550$ K gas respectively.

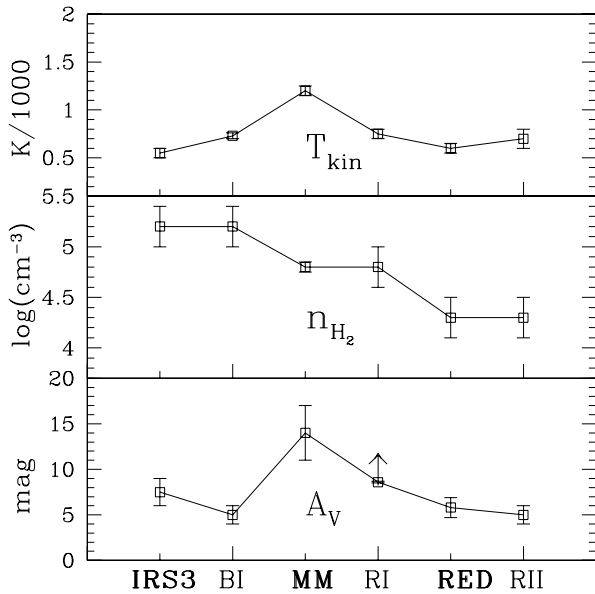


Fig. 10. Physical parameters (kinetic temperature, volume density and visual extinction) deduced from the analysis of the CO, H_2O and H_2 emission in the six positions pointed with ISO.

fact furtherly complicated by the tight blend of the $J=24$ and 23 lines with two backbone H_2O lines expected to be relatively strong. To separate the contributions from H_2O and CO, we have subtracted from the fluxes observed at 108.5 and $113.5\mu\text{m}$ the water line intensities as predicted by the model fitting the observed $174/179\mu\text{m}$ ratio with $T = 550$ K and $n = 2 \cdot 10^5 \text{ cm}^{-3}$. The

residuals are attributed to CO and are plotted in Fig. 9. We see from this figure that the so derived $J_{\text{up}}=23$ and 24 fluxes are still well above the fit obtained with the lower- J lines, indicating that a second component is really present. We can identify such a component as coming from the shocked gas strongly emitting in the H_2 $2.12\mu\text{m}$ line as evident in Fig. 1; such a gas is excited at high density with a temperature of about 2000 K (Davis & Smith 1995). In Fig. 9 we show the result of a convolution of the low and high temperature components. We note that the $J=25$ line is still much above the model at higher temperature; in fact this line cannot be consistently fitted with the other transitions for any value of temperature and density. We suppose that this line has been contaminated by the presence of a spurious signal not totally removed, as also suggested by the fact that the line center appears more than $0.3 \mu\text{m}$ apart from the vacuum wavelength of the CO line (see Table 2).

Fig. 10 summarizes the results obtained from the molecular analysis showing how the temperature, density and extinction are changing in the investigated regions along the flow. In addition to the already discussed behaviour of temperature and extinction, we also note that the density is decreasing from north to south, following the density structure of the cores in the region (B90). The emitting region sizes derived in the different positions (see Table 5) are always very compact, which suggests that the “warm” emission is correlated with the EHVs bullets all along the molecular jet and not only around the mm source. If so, the density of such bullets is not significantly enhanced with respect to the local density of the ambient medium. In particular, our derived values are about an order of magnitude lower than those estimated by mm observations alone both in CO and in SiO (B90, Bachiller et al. 1991). This is again a consequence of a much lower temperature assumed for the bullets by these authors with respect to the values derived here.

4. Discussion

4.1. Gas cooling along the flow

We are now able to derive all the energy radiated away along the outflow by the different species and to use these determinations both to estimate the global energy budget along the flow and to compare the different contributions with shock models.

The total cooling rates of CO, H_2 and H_2O have been computed from the derived model fits. For H_2 , in addition to the “warm” component as derived from the SWS observations, we also define a “hot” component which is traced by the ground based observations of the $2.12\mu\text{m}$ line at excitation temperatures of about 2000 – 3000 K (Davis & Smith 1995). The total cooling from this hotter gas has been derived by assuming that the total H_2 luminosity is ten times the luminosity in the $2.12\mu\text{m}$ line (which is approximately valid for a 2000 K gas in LTE). To compare this cooling with that of the other species, we have integrated the H_2 emission observed by Davis & Smith (1995) inside the LWS beam, and corrected it for the amount of extinction derived from our analysis.

Finally, the total cooling from atomic/ionic species, is directly given by the luminosity of their forbidden transitions ob-

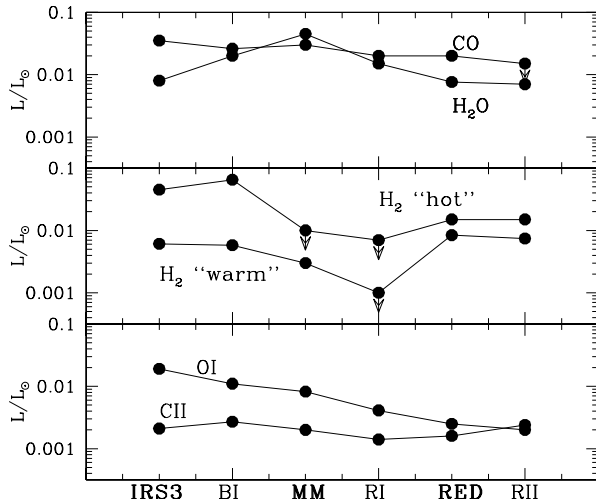


Fig. 11. Total luminosity emitted by the different molecular and atomic species detected along the L1448 outflow. “Warm” and “hot” H₂ refer to the H₂ traced by the (0–0) transitions observed with ISO-SWS and by the 2.12 μm line respectively.

served in our spectra, namely the 63 and 145 μm for O⁰, the 157 μm for C⁺ and the 35 μm for Si⁺, since these transitions represent the main cooling routes of these species in the physical conditions we are considering here. Table 6 lists all the derived cooling rates for the various investigated positions. We remind that the six LWS beams are strongly overlapping and therefore the various determinations based on LWS measurements can be compared only in a relative way to see the general trend along the flow. The total cooling for a species different from H₂ can be therefore evaluated by summing up the contributions from the ‘IRS3’, ‘mm’ and ‘RED’ pointings alone.

Having this caveat in mind, we show in Fig. 11 the luminosity radiated by the various gas components as a function of the position along the flow. There are a number of characteristics which are worth to be commented in this plot. First of all we notice that the C II emission is basically constant in all the investigated positions. As discussed in Paper I, such emission can be ascribed to the excitation due to the local interstellar field and thus not directly associated to the outflow.

There is an evident trend for O I and, to a lesser extent, also for CO emission to decrease from north to south. This behaviour can be due to the change in density along the flow, since the total luminosity directly scales with the density in optically thin regimes. Variations in abundance can however also contribute for the oxygen, since high temperature gas-phase reactions can easily incorporate much of the available oxygen into H₂O (see Sect. 4.4). The cooling due to water on the other hand, does not follow the same path: it has a maximum towards the mm source, where it has a value larger than for any other species, and decreases away from it. In fact it seems to be directly correlated with the temperature, which has a peak in the surroundings of the mm source.

Both the “warm” and “hot” H₂ emission seem to follow an opposite behaviour, showing a decrease of luminosity towards

the mm source. Given the different excitation conditions of these two components, such a decrease could indicate a lack of H₂ in the flow emanating close to the mm source, in other words a prevalence of hydrogen in atomic form in this region. More likely, since the “warm” gas observed by LWS is located in the high velocity bullets, the bulk of the “warm” H₂ emission has been missed by the loosely spaced SWS beams. The “hot” H₂ component, on the other hand, appears really missing towards the base of the flow from L1448-mm, unless our extinction values are heavily underestimated.

4.2. Global energy budget

From Fig. 11 and Table 6 we can see that no one of the different cooling species significantly prevails over the others. In general, the gas cooling is dominated by molecular emission and in particular the cooling due to the species traced by ISO contribute by more than 60% to the total gas cooling. If we just sum up all the luminosities derived for the various species, we find that the global gas cooling from L1448-mm and IRS3 and their outflows amount to about 0.3 L_⊙. An additional contribution is in fact expected from the “hot” gas component in the form of CO rotational emission with $J_{\text{up}} > 20$ (which we have only partially detected) and from CO vibrational transitions, which are expected to be excited for temperatures larger than 2000 K.

It is not easy to establish which part of this radiated power can be attributed to the L1448-mm and IRS3 flows separately, since the flow from IRS3 is totally embedded inside the blue lobe of the mm source outflow, and probably part of the radiated power also comes from the interaction of these two flows. The cooling from the mm source and its redshifted lobe alone, amount to 0.1 and 0.05 L_⊙ respectively. If we assume that the blueshifted part of the flow contributes to the total cooling as much as the red lobe, we can estimate that a total luminosity of about 0.2 L_⊙ is radiated from the L1448-mm outflow, and consequently the IRS3 source and its outflow contribute to about 0.1 L_⊙.

Assuming momentum balance in the shocked region between the stellar wind/jet and the ambient medium, Davis & Eisloffel (1996) derive the following relationship between the wind mechanical power L_w and the total power radiated by the shock L_{rad} :

$$\frac{L_{\text{rad}}}{L_w} = \frac{V_s}{V_w} \cdot \left(1 - \frac{V_s}{V_w}\right)^2 \quad (1)$$

where V_s and V_w are the shock and wind velocities respectively. If we assume for the mm source a shock velocity of $\sim 20 \text{ km s}^{-1}$ (see next section and Paper I) and a wind velocity of $\sim 150 \text{ km s}^{-1}$ (i.e. about the measured velocity of the molecular jet, corrected for an inclination of 70°, Dutrey et al. 1997), we derive a wind mechanical luminosity of about 3.5 L_⊙. This value is about 40% of the source bolometric luminosity, testifying for the large efficiency of the outflow as common among Class 0 sources. From this wind power, a mass loss rate value of about $1 \cdot 10^{-6} M_{\odot} \text{ yr}^{-1}$ can be derived. This is consistent with the wind mass loss rate which can be estimated from the CO

Table 6. Line cooling

| | IRS3 | BI | mm | RI | RED | RII | Total ^c |
|--------------------------------------|---------------------|----------------------|----------------------|----------------------|----------------------|----------------------|---------------------|
| | L/L_{\odot} | | | | | | |
| C ⁺ | $2.1 \cdot 10^{-3}$ | $2.7 \cdot 10^{-3}$ | $2.0 \cdot 10^{-3}$ | $1.4 \cdot 10^{-3}$ | $1.6 \cdot 10^{-3}$ | $2.4 \cdot 10^{-3}$ | $5.7 \cdot 10^{-3}$ |
| O ⁰ | $1.9 \cdot 10^{-2}$ | $1.1 \cdot 10^{-2}$ | $8.2 \cdot 10^{-3}$ | $4.1 \cdot 10^{-3}$ | $2.5 \cdot 10^{-3}$ | $2.0 \cdot 10^{-3}$ | $3.0 \cdot 10^{-2}$ |
| Si ⁺ | $1.6 \cdot 10^{-3}$ | $<6.6 \cdot 10^{-4}$ | $<8.0 \cdot 10^{-4}$ | $<8.0 \cdot 10^{-4}$ | $<7.2 \cdot 10^{-4}$ | $<5.5 \cdot 10^{-4}$ | $1.6 \cdot 10^{-3}$ |
| H ₂ (“hot”) ^a | $4.5 \cdot 10^{-2}$ | $6.5 \cdot 10^{-2}$ | $1.0 \cdot 10^{-2}$ | $7.0 \cdot 10^{-3}$ | $1.5 \cdot 10^{-3}$ | $1.5 \cdot 10^{-2}$ | $8 \cdot 10^{-2}$ |
| H ₂ (“warm”) ^b | $6.1 \cdot 10^{-3}$ | $5.8 \cdot 10^{-3}$ | $3.0 \cdot 10^{-3}$ | $1.0 \cdot 10^{-3}$ | $8.4 \cdot 10^{-3}$ | $7.4 \cdot 10^{-3}$ | $3.2 \cdot 10^{-2}$ |
| CO | $3.5 \cdot 10^{-2}$ | $2.6 \cdot 10^{-2}$ | $3.0 \cdot 10^{-2}$ | $2.0 \cdot 10^{-2}$ | $2.0 \cdot 10^{-2}$ | $<1.5 \cdot 10^{-2}$ | $8.5 \cdot 10^{-2}$ |
| H ₂ O | $8 \cdot 10^{-3}$ | $2.0 \cdot 10^{-2}$ | $4.5 \cdot 10^{-2}$ | $1.4 \cdot 10^{-2}$ | $7.6 \cdot 10^{-3}$ | $7.0 \cdot 10^{-3}$ | $6.0 \cdot 10^{-2}$ |

^a $L_{\text{tot}} = 10 \times L_{2.12 \mu\text{m}} \times 10^{A_k/2.5}$, where $L_{2.12 \mu\text{m}}$ is the luminosity in the 1-0S(1) line taken from Davis & Smith (1995) integrated inside the LWS beam and A_k is derived from an A_v obtained from the average of the values reported in Table 4.

^b Luminosity derived from our fit through the (0–0) lines.

^c For the species observed with LWS, the total luminosity has been computed by summing up only the values from the IRS3, mm and RED positions

outflow properties by B90 assuming momentum conservation. Our derived mechanical luminosity and mass loss rate are also in agreement with the values derived from the 2 cm radio continuum emission in the hypothesis of a pointlike optically thick ionized region (Curiel et al. 1990).

A different way to address this argument is to compute directly the momentum input rate of the molecular bullets closest to the mm source for which we can give a reliable mass estimate. Given our derived mass of $3 \cdot 10^{-3} M_{\odot}$, and assuming a bullet length of about $9 \cdot 10^{16}$ cm (i.e. about the observed $20''$ at 300 pc, de-projected for $\theta = 70^\circ$), we derive a jet mass input rate and mechanical luminosity of about $5 \cdot 10^{-6} M_{\odot} \text{ yr}^{-1}$ and $9 L_{\odot}$ respectively. This values are higher than the mass loss rate and luminosity derived above for all the outflow. This supports the hypothesis of episodic mass ejections in which the single and youngest jet bullet can bring a momentum larger than the value averaged on all the outflow history.

4.3. Prevailing shock conditions

In Paper I it has been suggested that the presence of a non-dissociative “Continuous” shock (C-shock, Draine 1980) with a velocity of about 20 km s^{-1} associated with the molecular bullets, can account for most of the observed characteristics of the gas emission in the surroundings of the L1448-mm source. Our JCMT observations reinforce these conclusions, showing that the CO 4-3 and 3-2 emission from the molecular bullets can be consistently fitted with the higher rotational number CO transitions.

The main argument adopted in Paper I to exclude a big contribution from a dissociative “Jump” shock (“J” shock, Hollenbach & McKee, 1989) was the inconsistency of the observed cooling ratios among the various observed species with the derived densities of the post-shocked gas, which would imply a prevailing atomic cooling. The same reasoning can be applied for the rest of the flow, with the possible exception of the IRS3 position which will be discussed below. In particular, moving away from the mm source we find that the “warm” component

tracing the molecular jet decreases in temperature and density, which indicate that the shock is propagating at slightly lower velocity into a more diffuse medium. This is in trend with the SiO map obtained by Dutrey et al. (1997) in the red counterflow, which shows that the velocity of the collimated jet is diminishing going from the mm source towards the red lobe apex.

The derived post-shock density in the various positions is not very different from the average cloud density, suggesting a small shock compression factor. The post-shock compression can be limited by the presence of strong magnetic fields; in particular, given a shock velocity of $\sim 20 \text{ km s}^{-1}$, a compression factor $n_{\text{post-shock}}/n_0$ of about 5, as suggested by our observations, implies the presence of a magnetic field component perpendicular to the shock velocity of the order of $300 \mu\text{G}$ (Hollenbach 1997). Since the magnetic field strength scales as the square root of the volume density (Troland & Heiles 1986), values up to 1 mG are expected to be found in dense environments and are actually deduced in shocked regions along dense flows (e.g. Chrysostomou et al. 2000).

The presence of a low velocity C-shock as the main excitation mechanism for the observed molecular gas, seems to contrast with the high velocity proper motion of the bullets of the order of 150 km s^{-1} . The discrepancy between high-velocity gas and low excitation is in fact a well known problem in shocked regions along molecular outflows. Typical examples are the H₂ near infrared jets which show proper motions well in excess of the $\sim 50 \text{ km s}^{-1}$ speed limit for the H₂ dissociation (see e.g. Chrysostomou et al. 2000). One way to overcome this discrepancy has been to assume that mass flows are variable in time and that the present jets are moving in a medium already put into motion by a previous event: in this way the shock velocity can be much lower than the actual velocity at which the jet is moving. Such an explanation can very well fit in the L1448 outflow, where the various bullets symmetrically displaced in the blue and red part of the flow strongly suggest an episodic ejection of matter.

An alternative possibility could be that the warm gas is originated in a turbulent mixing layer between the flow and the am-

bient medium (Cantó & Raga 1991). The chemical structure of the mixing layer which originates at the boundary between the stellar jet and the molecular environmental material has been modelled in details by Taylor & Raga (1995) who predict that in such a region warm molecular gas can survive at the high velocities characteristics of the jets. They however find that the gas temperature reaches values much higher ($\gtrsim 4000$ K) than the values deduced here and that the main cooling is achieved through H_2 , OH and partially CO, while H_2O never reaches abundances high enough to be a significant cooler, a result which clearly strikes against our observations.

From Fig. 1 we see that the morphology of the $2.12\mu\text{m}$ emission is not uniform along the outflow; in the red lobe it is much more patchy and weaker than in the blue lobe, where an arch-shaped structure typical of a bow shock is very clearly delineated. The excitation in a curved shock is in fact the most natural explanation for the presence of different excitation conditions like those testified by the “warm” and “hot” gas respectively (Smith 1994). We can however see from Figs. 1 and 11 that no $2.12\mu\text{m}$ emission is observed in the surroundings of the mm source, where at variance we measure a strong contribution especially from CO and H_2O . We can try here to delineate a possible picture for explaining the different excitation conditions on the L1448-mm flow. The molecular jet close to the mm source (traced by the R1 and B1 bullets) is the youngest and thus very fast and warm. There is no “hot” H_2 emission associated with it. This can be due to the larger extinction which prevents the detection of the $2.12\mu\text{m}$ line, or, alternatively it can be that these bullets are moving in a medium which has been already evacuated by the previous jets and thus they are not able to develop shocks strong enough to attain the higher temperatures needed to excite the H_2 vibrational transitions. The other bullets represent older episodes of mass loss which have already had time to cool and slow down. The blue lobe jet strikes directly against a high density medium creating the well defined and energetic bow shock clearly delineated by the H_2 $2.12\mu\text{m}$ emission. On the contrary, the bullets in the red lobe are moving through a medium where the density is decreasing and thus their associated bow shocks are not very energetic.

Going towards the northern outflow (IRS3), the shock conditions appear to slightly change. In the IRS3 position we note that, with respect to the mm source, there is a sharp decrease of the water emission, a maximum of O I, and the presence of Si II which is elsewhere not detected. All these evidences, and in particular the detected Si II line, suggest that an additional contribution to the gas excitation is here coming from a dissociative shock. The passage from a “C” shock to conditions favourable for a “J” shock can occur due to an increase in velocity or to a higher ionization fraction and less intense magnetic field. An oblique shock at higher velocity can be originated in the region where the flow from L1448-mm strikes against the IRS3 outflow; here the presence of a dissociative shock is also testified by the detection of the Herbig-Haro HH197 (coincident with the H_2 knots F,G and H of Fig. 1, Bally et al. 1997). Bally et al. claim that emission lines of [SII] and $\text{H}\alpha$ are also detected in the direction of the IRS3 reflection nebula, indicating shock excited

HH objects embedded in it; these high excitation spots could be also responsible for the Si II emission observed by us. The ratio $[\text{O I}] 63\mu\text{m}/[\text{Si II}] 35\mu\text{m}$ could be in principle used to infer the shock velocity and/or the pre-shock density by means of the current dissociative shock models (i.e. Neufeld & Dalgarno 1989; Hollenbach & McKee 1989). However, since the O I and Si II observed beams are so different and the region so crowded, the obtained ratio, which amounts to 11, can be considered only an upper limit to the real value. A lower limit of 1.5 can be instead obtained by assuming that the O I emission is uniformly distributed inside the LWS beam, and therefore correcting for the different beamsizes. In the Hollenbach & McKee model values as low as 10 for this ratio are attained only for very low values of the pre-shock densities ($n_o \lesssim 10^3 \text{ cm}^{-3}$) and $V_s < 50 \text{ km s}^{-1}$. On the other hand, the Neufeld and Dalgarno model, which makes a more complete treatment of the Silicon chemistry, predicts O I/Si II ratios in our derived range for all of their considered parameter space. We therefore conclude that the observed ratio is not able to constrain the physical parameters of this fast shock.

4.4. Shock enhanced water abundance

In cold molecular clouds, almost all water is depleted onto grains in the form of icy mantles. The gas-phase water abundance can be however largely enhanced both by evaporation from the grains and from gas-phase chemical reactions, these latter becoming efficient as soon as the gas temperature exceed ~ 300 K (Elitzur & de Jong 1978). In principle, these endothermic reactions could be able to convert into water all the available oxygen not locked in CO, causing the H_2O abundance to exceed a value of 10^{-4} . In practice, however, the amount of gaseous water can be easily diminished; this can be accomplished for example by the presence of UV photons which dissociate water in favour of OH, or if the medium is dense enough to have again a very quick depletion on dust grains (Bergin et al. 1998). The abundance of water is particularly high in L1448-mm compared to that measured in other low-mass protostars (see Paper I). This result has been interpreted as a consequence of the occurrence of multiple shocks over a short interval of time, which have prevented a rapid depletion onto grains. The investigation of a larger region done on this work shows that water abundance is maintained high all along the outflow even if there are variations among the various positions. The maximum abundance is found towards the mm-source where water also gives the main contribution to the gas cooling; an abundance as high as 10^{-4} is maintained in the redshifted lobe while towards IRS3 this value drops to about $3 \cdot 10^{-5}$. This last value is more in agreement with values derived for other young objects (see Paper I), confirming the peculiarity of L1448-mm as a strong water producer.

We can also compare the derived water enhancement with the behaviour of a similar shock molecular tracer like SiO. Shock reprocessing of dust can release SiO to the gas phase and the conditions for this process are very similar to those needed for the production of water molecules through gas-phase reactions (Schilke et al. 1997). SiO has been extensively observed

along L1448 and the molecular bullets originally detected in CO have been found to be strong SiO emitters (Bachiller et al. 1991; Dutrey et al. 1997). The SiO abundance derived in the various parts of the flow correlates with our derived H₂O values since the larger contribution has been found toward the bullets close to the mm source, while in the other parts of the flow a SiO abundance one order of magnitude lower is deduced (Bachiller et al. 1991). From an inspection of the SiO emission map in the various transitions (Fig. 2 of Bachiller et al. 1991) we also note that while the $J=2-1$ transition is widely emitted in all the bullets at about the same intensity levels, the higher excitation line $J=5-4$ appears to be very strong towards the mm source, less intense towards the red lobe and much fainter towards IRS3. This behaviour very closely resembles the water emission observed by us, indicating that there is a tight correlation between the warm H₂O and the SiO emission at high excitation. This last result contrasts with the finding by Ceccarelli et al. (1999), who find no correlation between water and SiO emission for a sample of young stellar objects. However, given the fact that the water lines detected by LWS probe only warm gas (i.e. gas with $T > 100$ K), the inclusion by these authors of the emission from all the SiO observed transitions, irrespective of their excitation, can cause an alteration of the resulting correlation if strong temperature gradients are present.

5. Conclusions

We have presented the results of a far infrared detailed study conducted along the molecular outflows from L1448-mm and L1448-IRS3 with the spectrometers on board the ISO satellite. These observations have allowed to define the main cooling channels of the shock excited gas in different positions of the flow and thus to give an evaluation of the energy radiatively lost with an accuracy that we cannot achieve from ground based observations only.

We derive that more than 60% of the gas cooling occurs through emission of pure rotational lines from CO, H₂O and H₂ excited at temperatures between 500 and 1200 K, while the rest of the energy is radiated mainly in the hotter gas (at $T \sim 2000$ K) traced by the H₂ 2.12 μ m line and in the [O I] 63 μ m line. Additional observations of the ¹²CO 4-3 and 3-2 transitions conducted with the JCMT in the surroundings of the L1448-mm source have allowed us to localize this warm emission in the extreme high velocity clumps displaced along the outflow axis to form a molecular jet, which are supposed to represent different episodes of mass loss from the central protostar. Our analysis shows therefore that this molecular jet is much hotter than previously thought on the basis of millimeter observations alone, and consequently the mass derived for the single clumps are higher than the estimates given in the past.

A comparison with existing models suggests that the excitation along the outflow from L1448-mm is mainly due to low velocity ($V_s \leq 20$ km s⁻¹) non-dissociative shocks (C-shocks) developed in a medium where the magnetic field component perpendicular to the shock velocity is $\sim 300 \mu$ G. Excitation from turbulent mixing layers along the molecular jet axis seems less

suitable in explaining the observed cooling ratios among the different molecular components and the derived gas temperature. In the direction of the source L1448-IRS3 the emission is characterized by a higher excitation, as testified by the detection of the [Si II] 35 μ m line and by a larger contribution to the cooling due to the O I emission. Here, it is likely that a dissociative shock (J-shock) is also present, which could be located in the region of interaction between the outflows from the two sources, where also optical HH objects have been detected.

Finally, the abundance of water, which reaches a value as high as $5 \cdot 10^{-4}$ towards the mm source, is maintained high along the red-shifted part of the outflow, while drops to a value of about 10^{-5} towards the IRS3 source. A comparison with a map of the region in the SiO 5-4 emission shows that the water emission is strongly correlated with SiO at high excitation implying that gas-phase water and SiO are both released in the low-velocity shocks developed along the outflow.

Acknowledgements. We would like to thank the JCMT staff for their support during the observations. The James Clerk Maxwell Telescope is operated by the Joint Astronomy Centre on behalf of the Particle Physics and Astronomy Research Council of the United Kingdom, the Netherlands Organization for Scientific Research, and the National Research Council of Canada.

References

- André P., Ward-Thompson D., Barsony M., 2000, In: Mannings V., Boss A.P., Russell S.S. (eds.) *Protostars and Planets IV*
- Bachiller R., Chernicharo J., Martín-Pintado J., Tafalla M., Lazareff B., 1990, *A&A* 231, 174 (B90)
- Bachiller R., Martín-Pintado J., Fuente A., 1991, *A&A* 243, L21
- Bachiller R., Guilloteau S., Dutrey A., Planesas P., Martín-Pintado J., 1995, *A&A* 299, 857
- Bally J., Lada E.A., Lane A.P., 1993, *ApJ* 418, 322
- Bally J., Devine D., Alten V., Sutherland R.S., 1997, *ApJ* 478, 603
- Barsony M., Ward-Thompson D., André P., O'Linger J., 1999, *ApJ* 509, 733
- Benedettini M., Giannini T., Nisini B., et al., 2000, *A&A* 359, 148
- Bergin E.A., Melnick G.J., Neufeld D.A., 1998, *ApJ* 499, 777
- Cantó J., Raga A.C., 1991, *ApJ* 372, 646
- Ceccarelli C., Caux E., Loinard L., et al., 1999, *A&A* 342, L21
- Chandler C.J., Richer J.S., 2000, *ApJ* 530, 851
- Chernin L.M., 1995, *ApJ* 440, L97
- Chernin L.M., Masson C.R., 1995, *ApJ* 455, 182
- Chrysostomou A., Hobson J., Davis C.J., Smith M.D., Berndsen A., 2000, *MNRAS* 314, 229
- Curiel S., Raymond J.C., Rodriguez L.F., Cantó J., Moran J.M., 1990, *ApJ* 365, L85
- Clegg P.E., Ade P.A.R., Armand C., et al., 1996, *A&A* 315, L38
- Davis C.J., Eisloffel J., 1996, *A&A* 305, 694
- Davis C.J., Smith M., 1995, *ApJ* 443, L41
- Davis C.J., Dent W.R.F., Matthews H.E., Aspin C., Lightfoot J.F., 1994, *MNRAS* 266, 933
- de Graauw T., Haser L.N., Beintema D.A., et al., 1996, *A&A* 315, L49
- Draine B.T., 1980, *ApJ* 241, 1021
- Draine B.T., 1989, In: *Infrared Spectroscopy in Astronomy*. ESA SP-290, p. 93
- Dutrey A., Guilloteau S., Bachiller R., 1997, *A&A* 325, 758
- Eisloffel J., 2000, *A&A* 354, 236

- Elitzur M., de Jong T., 1978, *A&A* 67, 323
- Hatchell J., Fuller G.A., Ladd E.F., 1999, *A&A* 346, 278
- Hollenbach D., 1997, In: Reipurth B., Bertout C. (eds.) *Herbig-Haro flows and the birth of low mass stars*. IAU Symposium no. 182, p. 181
- Hollenbach D., McKee C.F., 1989, *ApJ* 342, 306
- Kessler M.F., Steinz J.A., Anderegg M.E., et al., 1996, *A&A* 315, L27
- Liseau R., Ceccarelli C., Larsson B., et al., 1996, *A&A* 315, L181
- Neufeld D.A., Dalgarno A., 1989, *ApJ* 340, 869
- Nisini B., Giannini T., Molinari S., et al., 1998, In: Yun J.L., Liseau R. (eds.) *Star Formation with the Infrared Space Observatory*. ASP Conference Series vol. 132, p. 256
- Nisini B., Benedettini M., Giannini T., et al., 1999a, *A&A* 343, 266
- Nisini B., Benedettini M., Giannini T., et al., 1999b, *A&A* 350, 529 (Paper I)
- Raga A., Cabrit S., 1993, *A&A* 278, 267
- Reipurth B., Raga A.C., 1999, In: Lada C.J., Kylafis N.D. (eds.) *The Origin of Stars and Planetary Systems*. p. 267
- Rieke G.H., Lebofsky M.J., 1985, *ApJ* 288, 618
- Schilke P., Walmsley C.M., Pineau des Forêts G., Flower D.R., 1997, *A&A* 321, 293
- Smith M.D., 1994, *MNRAS* 266, 238
- Swinyard B.M., Clegg P.E., Ade P.A.R., et al., 1996, *A&A* 315, L43
- Taylor S.D., Raga A.C., 1995, *A&A* 296, 823
- Terebey S., Padgett D.L., 1997, In: Reipurth B., Bertout C. (eds.) *Herbig-Haro flows and the birth of low mass stars*. IAU Symposium no. 182, p. 507
- Troland T.H., Heiles C., 1986, *ApJ* 301, 339
- Turner J., Kirby-Docken K., Dalgarno A., 1977, *ApJS* 35, 281